# ZnO/CuO Heterojunction Branched Nanowires for Photoelectrochemical Hydrogen Generation

Alireza Kargar,[†] Yi Jing,[†] Sung Joo Kim,[‡] Conor T. Riley,[§] Xiaoqing Pan,[‡] and Deli Wang[†,⊥,‖,*]

[†]Department of Electrical and Computer Engineering, University of California—San Diego, 9500 Gilman Drive, La Jolla, California 92093, United States, [‡]Department of Materials Science and Engineering, University of Michigan, 2300 Hayward Street, Ann Arbor, Michigan 48109, United States, [§]Department of Nanoengineering, University of California—San Diego, 9500 Gilman Drive, La Jolla, California 92093, United States, [⊥]Materials Science and Engineering Program, University of California—San Diego, 9500 Gilman Drive, La Jolla, California 92093, United States, and [‖]Qualcomm Institute, University of California—San Diego, 9500 Gilman Drive, La Jolla, California 92093, United States

ABSTRACT We report a facile and large-scale fabrication of three-dimensional (3D) ZnO/CuO heterojunction branched nanowires (b-NWs) and their application as photocathodes for photoelectrochemical (PEC) solar hydrogen production in a neutral medium. Using simple, cost-effective thermal oxidation and hydrothermal growth methods, ZnO/CuO b-NWs are grown on copper film or mesh substrates with various ZnO and CuO NWs sizes and densities. The ZnO/CuO b-NWs are characterized in detail using high-resolution scanning and transmission electron microscopies exhibiting single-crystalline defect-free b-NWs with smooth and clean surfaces. The correlation between electrode currents and different NWs sizes and densities are studied in which b-NWs with longer and denser CuO NW cores show higher photocathodic current due to enhanced reaction surface area. The ZnO/CuO b-NW photoelectrodes exhibit broadband photoresponse from UV to near IR region, and higher photocathodic current than the ZnO-coated CuO (core/shell) NWs due to improved surface area and enhanced gas evolution. Significant improvement in the photocathodic current is observed when ZnO/CuO b-NWs are grown on copper mesh compared to copper film. The achieved results offer very useful guidelines in designing b-NWs mesh photoelectrodes for high-efficiency, low-cost, and flexible PEC cells using cheap, earth-abundant materials for clean solar hydrogen generation at large scales.
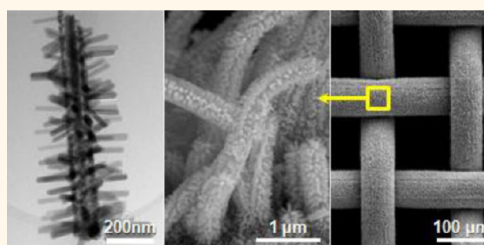
KEYWORDS: photoelectrochemical cell · solar water splitting · CuO · ZnO · branched nanowires (b-NWs)

The photoelectrochemical (PEC) water splitting for clean and practical hydrogen production requires cheap, efficient, and stable semiconductor photoelectrodes to split water and consequently generate hydrogen at large scales. Among the vast majority of studied materials so far, semiconductor metal oxides (Fe_2O_3, TiO_2, WO_3, ZnO, Cu_2O, and CuO) have shown promising potentials,[1−13] which are abundant, cheap, nontoxic, and can be fabricated using facile, cost-effective, and scalable fabrication techniques, such as hydro/solvothermal growth method[4,5,9,10] and electrodeposition.[1,7] Despite their potential for high solar-to-hydrogen (STH) conversion efficiencies,[1,5,14] there are several limiting factors, such as short diffusion length,[5,15−17] low conductivity,[9,18,19] and poor surface evolution kinetics,[20,21] that cause the STH efficiencies to be considerably lower than the predicated theoretical values.[2,4,5,9,10]

The formation of nanostructured metal oxides reduces the carrier diffusion length and increases the reaction surface area as well as improves the surface evolution kinetics.[22] Specifically, vertical metal oxide NWs have shown promising performances for the PEC solar water splitting because they provide enhanced light absorption, increased surface area, reduced carrier recombination, and improved charge collection efficiency.[4,6,9−11,19,23,24] Intrinsically n-type metal oxide NWs (Fe_2O_3,[2,9,19] TiO_2,[3,10] WO_3,[4,5,25] and ZnO[6,23]) have mostly been studied for the oxygen generating photoanode materials.[4,9,10,19,23] Copper oxides (CuO and Cu_2O) are the most studied metal oxides for the photocathodic hydrogen production as they are naturally p-type with proper band gaps for light absorption (E_g (CuO) $\cong$ 1.4 eV,[26] E_g (Cu_2O) $\cong$ 2 eV).[1,7,11,12,27,28] The formation of NW heterostructures can

enhance the PEC performance of copper oxide photocathodes resulting in an improvement of their STH efficiency due to increased charge separation and enlarged reaction surface area/sites. Furthermore, stable materials such as TiO_2 that are coupled with the copper oxides in the heterostructure, can improve the stability of copper oxide photocathodes because they can protect the surface of copper oxide electrodes against decomposition/corrosion in the electrolyte.[29]

Compared to core/shell NW (cs-NW) heterostructures, branched NWs (b-NWs) are very promising for PEC solar hydrogen production[30−32] due to enhanced surface area, improved light absorption,[22,33] and increased gas evolution.[22] In addition, the smaller size of the NW branches (compared to the size of NW cores) can also result in more efficient charge separation and collection due to the close proximity between the photogenerated carriers and the semiconductor-electrolyte interface.[24] We have recently demonstrated the ZnO/Si b-NW heterostructures for efficient solar water splitting and photocathodic hydrogen production,[22,31] which also provide tunable PEC performance resulting in selective water oxidation or reduction.[32] There are several reports for all-metal-oxide NW heterostructures for photoanode materials; however, to the best of our knowledge, there is no report employing all-metal-oxide NW heterostructures for photocathode materials for hydrogen production.[34,35] Having a b-NW heterostructure based on CuO and ZnO metal oxides can be a promising candidate for the photocathodic hydrogen production because it uses advantages of both CuO and ZnO[23,36] metal oxides for the solar water splitting as well as the aforementioned beneficial characteristics of the heterojunction b-NWs. Furthermore, such a b-NW structure is easily synthesized using facile, cost-effective and scalable fabrication methods such as thermal oxidation and hydrothermal growth.[37] The b-NWs based on all-metal-oxide NWs can also be used for other device applications such as lithium-ion batteries (LIBs),[38] and optoelectronic devices.[39]

In this paper, we present the facile and large-scale fabrication of 3D ZnO/CuO b-NW heterojunction photocathodes for PEC solar hydrogen production. The ZnO/CuO b-NWs are synthesized on different copper substrates, including copper foils and meshes, for different ZnO and CuO NWs sizes and densities. High-resolution scanning and transmission electron microscopies are employed to characterize the b-NWs in detail. The ZnO/CuO b-NWs are used as photocathodes and the correlation between the electrode currents and different NWs sizes and densities are studied. The spectral incident photon-to-current efficiency (IPCE) of the ZnO/CuO b-NW photoelectrodes is also investigated. An energy band diagram of the ZnO/CuO heterojunction b-NW is also proposed to help illustrating the working mechanism of the ZnO/CuO b-NWs.

RESULTS AND DISCUSSION

CuO NW arrays were synthesized on copper foil and mesh using the thermal oxidation growth method for different growth annealing times and temperatures (see the Methods for details). After the CuO NW growth, a thin ZnO layer as seeding layer for the ZnO NW growth was deposited on the as-grown CuO NW substrates by RF magnetron sputtering. The ZnO NW branches were finally grown on the CuO NW cores using the hydrothermal growth method. A three electrodes configuration (sample as working electrode (WE), Pt coil as counter electrode (CE), and Ag/AgCl (1 M KCl) as reference electrode (RE)) placed in 400 mL of a neutral aqueous electrolyte (0.25 M Na_2SO_4 buffered at pH = 7.25) was used to perform the current density measurements (see the Methods for more details). A constant light power intensity of ∼109 mW/cm^2 was tuned on the samples. The spectral photoresponse and incident photon-to-current efficiency (IPCE) measurements were carried out using the same setup and electrolyte as described for the current density measurements. For convenience, ZnO/CuO b-NW arrays for different ZnO NW growth times, and different CuO NW growth annealing times and temperatures are denoted as "b(Xm-ZnO/Yh-Z°C-CuO) NWs". "X", "Y", and "Z" are the ZnO growth time in minutes (m), growth annealing time in hours (h), and growth annealing temperature, respectively (for example, "5m-ZnO" means ZnO NWs grown for 5 min or "3h-400°C-CuO" means CuO NWs grown for 3 h at 400 °C.

Figure 1 exhibits the scanning electron microscopy (SEM) images of the CuO NW arrays grown on Cu foil for different annealing times (2, 3, 4, or 5h) and temperatures (400, 450, or 500 °C). Longer annealing time results in larger average diameter and length (Figure 1a−d), higher density (Figures S1a−d), and darker sample color (see optical images in the insets of Figure 1a−d). The growth of CuO NWs is uniform through the whole area of samples as can be seen by the optical images in the insets of Figure 1a−d and low-magnification SEM image in Figure S1e. The CuO NW growth mechanism involves two steps:[40]

$$4Cu + O_2 \rightarrow 2Cu_2O \qquad (1)$$

$$2Cu_2O + O_2 \rightarrow 4CuO \qquad (2)$$
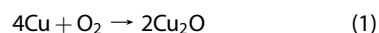
In the first step (eq 1), a Cu_2O layer forms on the surface of copper substrate which serves as the precursor for the CuO growth in the second step (eq 2). The CuO NWs are then formed through rapid and short-circuit diffusion of Cu ions across grain boundaries and/or defects in the Cu_2O layer.[41] This is evident by the observation of three different parallel copper oxide layers on the copper substrate (Figure S2a), including Cu_2O film, CuO layer, and CuO NW array. The order of copper oxide layers on the Cu substrate can also be explained by the diffusion theory in which Cu_2O with higher Cu concentration than CuO is the closest layer to the Cu substrate.[26] The thickness of CuO film underneath the
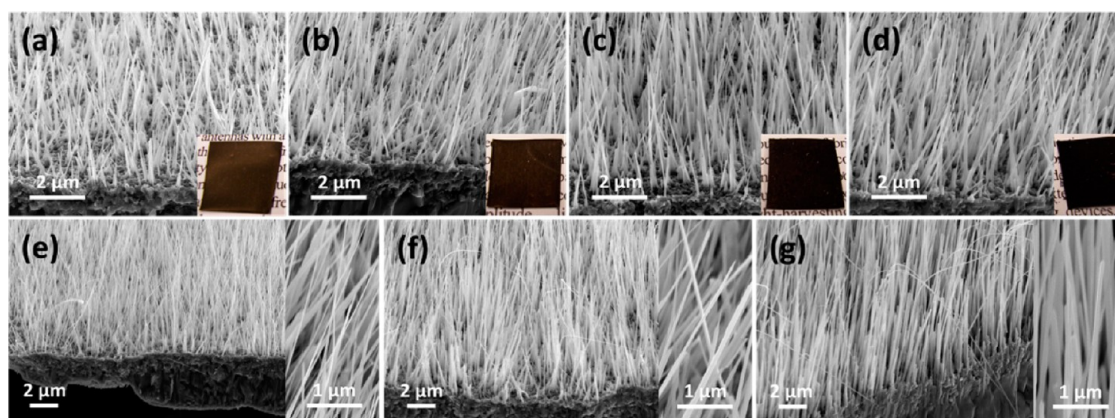
Figure 1. SEM images of CuO NW arrays grown at 400 °C on Cu foil for different annealing times: (a) 2, (b) 3, (c) 4, and (d) 5 h. The insets show the optical images of the corresponding samples. SEM images of CuO NWs grown for 4 h on Cu foil at different annealing temperatures: (e) 400, (f) 450, and (g) 500 °C. The insets show the high-magnification images of the corresponding samples.

CuO NW layer increases with increasing the annealing time (Figure S2b–d), consistent with longer CuO NWs for longer annealing time. Higher temperature results in larger average length and diameter (insets of Figure 1e–g), and lower NW density (Figure S1f–h). In addition, at higher temperature, bending is observed due to the high aspect ratio of the NWs.

Low-magnification bright field (BF) transmission electron microscopy (TEM) image of a single 4h-400°C-CuO NW is shown in Figure 2a, exhibiting a diameter of ~55 nm. The CuO NWs show different diameters and lengths for one specific growth temperature and time as shown in TEM (Figure S3) and SEM (Figure 1) images. By examining different CuO NWs (see Figure S3), we can conclude that they are rather defect free. A partly magnified TEM image of the CuO NW along its length further reveals the quite defect-free structure (Figure S4). The high-resolution TEM (HRTEM) image (Figure 2b) exhibits the single-crystalline nature of CuO NW. The calculated lattice spacing is ~0.27 nm corresponding to (110) plane of monoclinic CuO, which is consistent with that reported elsewhere for the CuO NWs synthesized with the same method.[11,26] The fast Fourier transform (FFT) pattern of the HRTEM image shows CuO single crystallinity oriented along the (111) direction indicating a growth direction of [111]. In addition, the NW surface is smooth without any amorphous layer. The partly magnified TEM image in Figure S4 also shows that the CuO NW has smooth surfaces along its entire length though there is an amorphous layer in some parts which can be due to either long exposure of NWs in air or contamination from the microscope. Low-magnification high angle annular dark field (HAADF) scanning transmission electron microscopy (STEM) image of a similar-sized CuO NW is shown in Figure 2c. High-resolution annular bright field (ABF) STEM images of left and right sides of NW clearly reveal the CuO NW single crystallinity.

Figure 3a,b shows 4h-400°C-CuO NWs grown on Cu mesh with ZnO seeding layer coating. After the ZnO
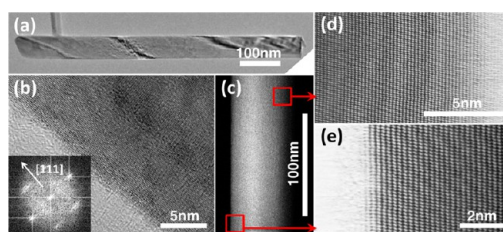

Figure 2. (a) Low-magnification bright field TEM image of a single 4h-400°C-CuO NW and (b) high-resolution TEM image of left side of corresponding CuO NW. Inset shows the calculated FFT pattern indicating the CuO NW growth direction. (c) Low-magnification high angle annular dark field STEM image of a similar-sized CuO NW. (d and e) High-resolution annular bright field STEM images of NW sides.

seeding layer deposition, longer CuO NWs bend. The ZnO/CuO b-NW arrays on Cu foil with 3h-400°C-CuO NW cores, and different ZnO NW branches are shown in Figure 3c–h. For different ZnO growth times, ZnO NWs grow through the entire length of CuO NW cores due to the conformal coating of ZnO seeding layer. There is ZnO NW growth in spaces between CuO NWs on flat surface since the ZnO seeding layer covers all surfaces on the substrate. Longer ZnO growth time results in longer ZnO NW branches. Besides the growth time, the size of ZnO NW branches can be tuned by altering the precursor concentrations for ZnO growth.[39] After the ZnO NW growth, longer CuO NW cores bend and bending increases with longer ZnO growth time (Figure S5 and Figure 3). The growth of ZnO/CuO b-NWs is through the entire area of samples and it is not limited to the small parts.

Figure 4a shows low-magnification ABF STEM image of a single ZnO/CuO b-NW clearly exhibiting three different regions including CuO NW core, ZnO seeding layer, and ZnO NW branches. There is formation of an amorphous layer in interface between CuO NW and ZnO seeding layer (see also annular dark field (ADF) STEM images in Figure S6 to better observe such a layer as well as three different regions). The formation of such an amorphous layer is throughout the entire length of the CuO NW (Figure S6). HAADF STEM image
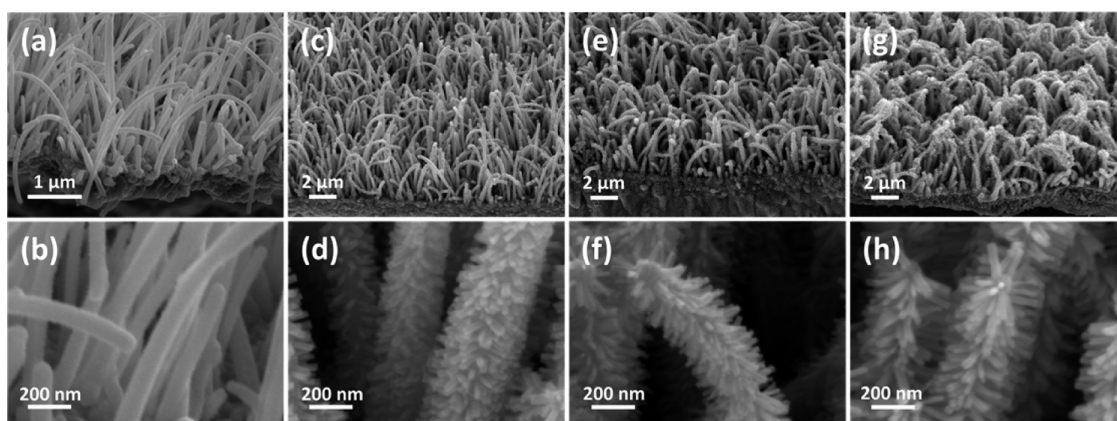
Figure 3. (a−b) SEM images of 4h-400°C-CuO NWs on Cu mesh with ZnO seeding layer. SEM images of ZnO/CuO b-NWs on Cu foil with 3h-400°C-CuO NW cores, and different ZnO NW branches ((c and d) 5m-ZnO, (e and f) 10m-ZnO, (g and h) 15m-ZnO).
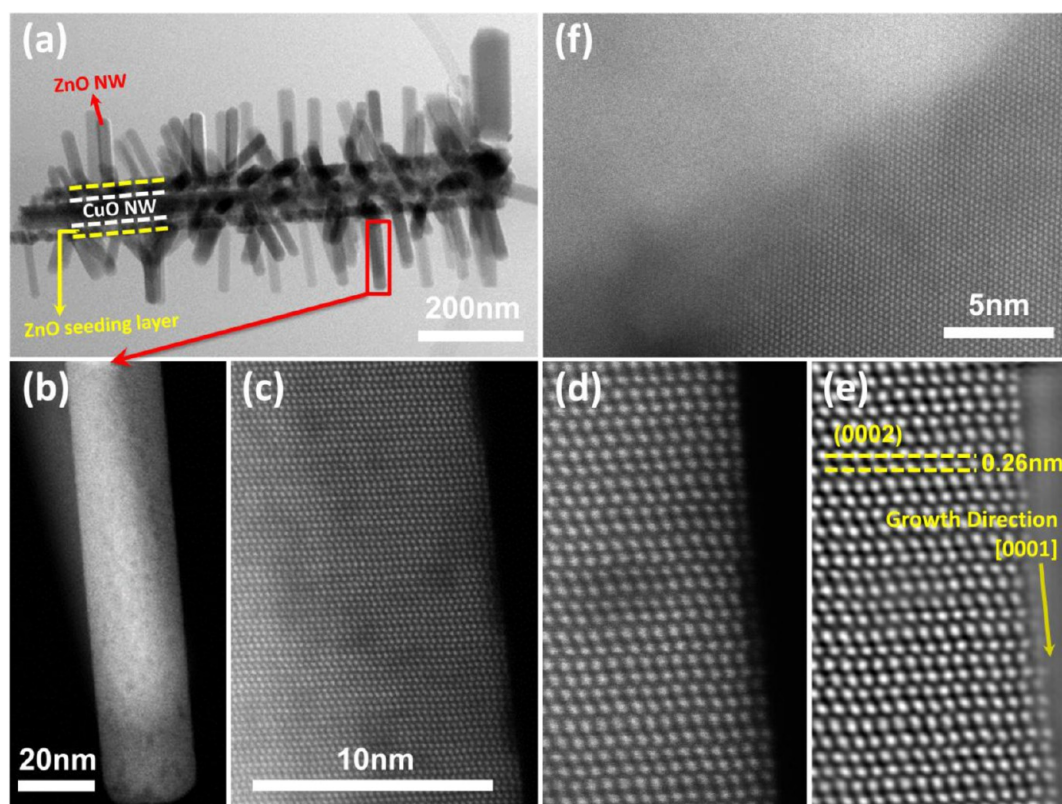

Figure 4. (a) Low-magnification annular bright field STEM image of a single b(10m-ZnO/4h-400°C-CuO) NW. (b) High angle annular dark field STEM image of labeled single ZnO NW. (c and d) High-resolution images of right side of ZnO NW in (b). (e) The corresponding noise-filtered image of (d). (f) High-resolution high angle annular dark field STEM image of interface between a ZnO NW and ZnO seeding layer from a b-NW shown in Figure S7.

of a single ZnO NW with ∼25 nm diameter, selected from Figure 4a, is shown in Figure 4b. The brighter portion is due to overlap from another ZnO NW sitting on the back of this ZnO NW (see Figure S6). High-resolution HAADF STEM images (Figure 4c,d) indicate that the ZnO NW is comprised of the single crystal wurtzite structure, and defect free with smooth and clean surfaces. The modified image of high-resolution HAADF STEM image *via* noise filtering (Figure 4e) exhibits a lattice spacing of ∼0.26 nm along (0002)

plane, which is consistent with that reported elsewhere for the ZnO NWs grown with the same method.[42] The ZnO growth direction for this selected ZnO NW is along [0001] (*c*-direction). Figure 4f shows a high-resolution HAADF STEM image of interface between ZnO NW and ZnO seeding layer. Note that it is hard to clearly see the crystal structure of the ZnO seeding layer due to the overlap of many NWs with the seeding layer. The actual thickness of the ZnO seeding layer on the CuO NW (see Figure S7) is ∼30 nm, which is less than half of
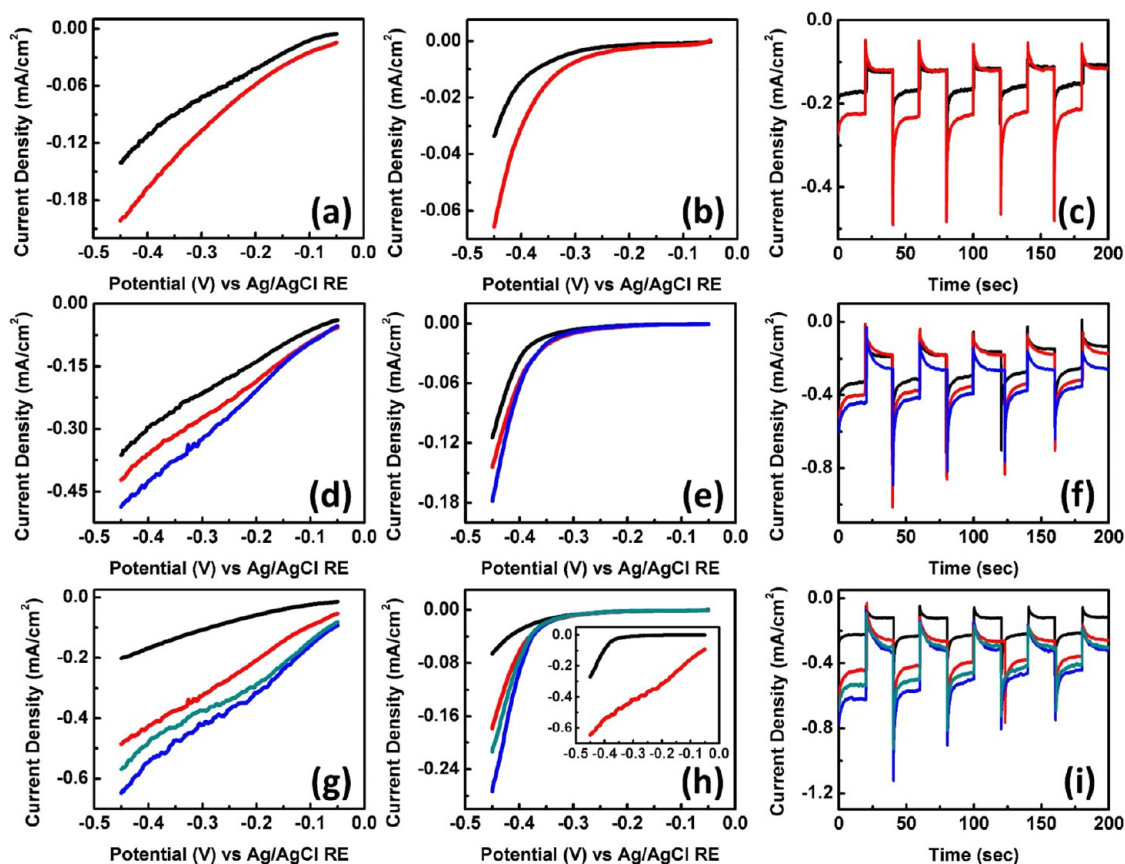
Figure 5. Current density of CuO/ZnO cs-NWs grown at 400 °C for different annealing times (black line, 2 h; red line, 5 h) on Cu foil (a) under light illumination and (b) at dark. (c) Transient current density under chopped illumination of the corresponding samples. Current density of 5m-ZnO NWs on CuO NW cores grown at 400 °C for different annealing times (black line, 2 h; red line, 4 h; blue line, 5 h) on Cu foil (d) under light illumination and (e) at dark. (f) Transient current density under chopped illumination of the corresponding samples. Current density of 5h-400°C-CuO NW cores on Cu foil with different ZnO NW branches (black line, ZnO seeding layer; red line, 5m-ZnO; blue line, 10m-ZnO; dark cyan line, 15m-ZnO) (g) under light illumination and (h) at dark. The inset in (h) shows the dark (black line) and light (red light) currents for 10m-ZnO NWs on 5h-400°C-CuO NW cores. (i) Transient current density of the corresponding samples. The applied external bias for all the transient current densities in (c), (f), and (i) is −0.5 V versus Ag/AgCl RE.

predicted deposition thickness (see the Methods) due to the high surface area of CuO NWs. Besides the ZnO NWs with crystallographic orientation of [0001] shown in Figures 4d ,e, we have also observed ZnO NWs with [110] growth orientation, identified with the ⟨0001⟩ zone axis (see Figure S8).

The current density measurements in a neutral solution of ZnO/CuO b-NWs on Cu foil for different CuO growth annealing and ZnO growth times are shown in Figure 5. Figure 5a,b exhibits the $J-V$ measurements for the ZnO-seeding-layer-coated CuO NWs (CuO/ZnO core/shell NWs (cs-NWs)) grown at 400 °C for different annealing times, showing a photocathodic behavior due to the p-type nature of the CuO NWs (see the Supporting Information and Figure S9 for the p-type conductivity). The dark and light currents increase with longer annealing time due to the increased reaction surface area. In addition, the CuO NWs grown with longer annealing time provide higher absorption (see optical images in the insets of Figure 1a−d), allowing higher photocathodic current. Figure 5c illustrates the transient current density under chopped

illumination for the corresponding cs-NWs at −0.5 V exhibiting good switching behavior.

The effect of CuO growth annealing time on the light and dark currents of ZnO/CuO b-NWs are exhibited in Figure 5d,e. The ZnO/CuO heterojunction b-NWs also show photocathodic behavior. Longer annealing time results in higher dark and light currents due to the enhanced surface area and probably increased optical absorption which can come from the improved light trapping of longer NWs.[43] The trends for different annealing times in the transient current density (Figure 5f) confirm the trends in Figure 5d,e. Figure 5g,h shows the effect of ZnO NW growth time on the light and dark currents of b-NWs. The ZnO/CuO b-NWs show higher light and dark currents than the CuO/ZnO cs-NWs resulting in improved photocathodic current which can be due to the increased reaction surface area and enhanced gas evolution as a result of the large curvature of ZnO NWs.[22,32] The ZnO/CuO b-NWs with 10m-ZnO NWs exhibit the highest dark and light currents between the investigated b-NWs. Despite the higher surface area of b-NWs with 15m-ZnO NWs, they show lower dark and light

currents than the b-NWs with 10m-ZnO NWs. This may be due to the increased bending of b-NWs with 15m-ZnO NWs (Figures S5 and Figure 3), which may reduce the effective area for surface reactions leading to lower dark and light currents. The trends for different ZnO growth times in the transient current density (Figure 5i) confirm the observed trends in Figure 5g,h. As shown in Figure 5f,i, the b-NWs show good switching behavior for different CuO growth annealing and ZnO growth times. The photocathodic current overshoots in the beginning of switching light on in Figure 5c,f,I can be due to the accumulation of photogenerated carriers at the interface between NWs and electrolyte, and consequent recombination until reaching a stationary photocurrent. Note that there are also current overshoots under switching off though their magnitude is much smaller. Note that the shapes of dark and light currents in the $J-V$ plots for the cs-NWs and b-NWs (Figure 5) are similar to that reported for the CuO film photocathodes.[13]

The approximate energy band diagram of the ZnO/CuO heterojunction b-NW in contact with the electrolyte at a reversed biasing potential of -0.45 V is shown in Figure 6. For the junction between p-CuO and n-ZnO NWs, the depletion region mostly lies in the p-CuO NW due to much higher doping concentration of n-ZnO NW, which is in the order of 10^{18} cm^{-3} for the ZnO NW grown by the hydrothermal growth method.[44] The calculated doping concentration for the p-CuO NW is about 9×10^{16} cm^{-3} (see the Supporting Information), which is in the range of that reported elsewhere.[41] Furthermore, in general, the radius of CuO NW core is smaller than the length of ZnO NW branch (see Figure 6 inset and Figures 3 and 4). These two factors cause a large band bending in the CuO NW core to occur. The considered band gaps for CuO and ZnO NWs are 1.4 eV[26] and 3.4 eV, respectively. The energy levels of bottom of the conduction band (CB) for the CuO and ZnO are estimated to be 4.07 and 4.35 eV,[45,46] respectively, resulting in the estimated values of 0.28 and 1.72 eV for the ΔE_{CB} and ΔE_{VB}, respectively, under the thermal equilibrium condition. Under light illumination, there is a small photocurrent at around zero biasing potential (see Figure 5h inset for a photocurrent of 0.09 mA/cm^2 at -0.05 V) due to photogenerated carriers coming from the CuO-ZnO and ZnO-electrolyte junctions. By increasing the reversed biasing potential, the energy levels of ZnO move downward resulting in more band bending at the CuO-ZnO junction (the junction becomes more favorable and effective for charge separation and transport) and reduced barrier at the ZnO-electrolyte junction (see Figure 6). These increased band bending and decreased barrier lead to the enhanced light current.

To further evaluate the performance of ZnO/CuO b-NWs, the spectral IPCE of b(5m-ZnO/3h-400 °C-CuO) NWs at -0.4 V is presented in Figure 7. From 450 to 500 nm, there are IPCEs larger than 8% with a maximum efficiency of 10%. The ZnO/CuO b-NWs
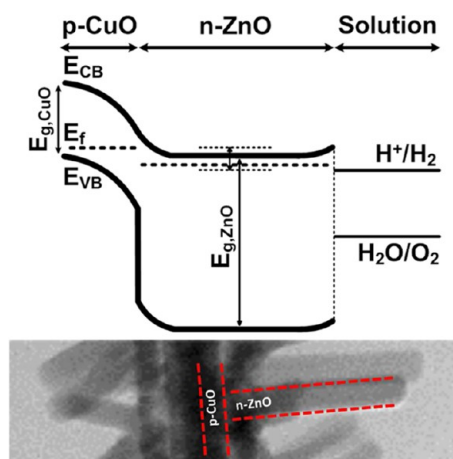

Figure 6. Approximate energy band diagram of the ZnO/CuO heterojunction b-NW in contact with the electrolyte at a reversed biasing potential of -0.45 V. The inset shows a STEM image (part of Figure 4a) indicating the relative size of the CuO NW radius to the ZnO NW length.
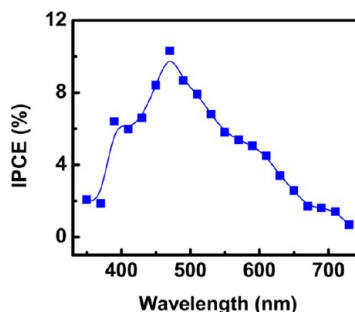

Figure 7. Spectral incident photon-to-current efficiency (IPCE) of b(5m-ZnO/3h-400°C-CuO) NWs at -0.4 V versus Ag/AgCl RE.

show broadband photoresponse from UV to near IR region due to coupling of low band gap CuO with high band gap ZnO. The 4h-450°C-CuO NW shows a field effect mobility of 0.0052 cm^2/(V·s) (see Figure S9 and mobility calculation in the Supporting Information), which is much higher than reported before.[41] Although mobility of the CuO NWs grown by the applied thermal oxidation method is very low which affects the PEC performance shown in Figure 5, the PEC performance can significantly be enhanced by increasing the effective surface area. The CuO NWs on Cu mesh provide much higher surface area than that on Cu foil, in which the surface area enhancement has been estimated to be 135%.[47] Note that this estimated value can vary for different meshes with different diameter and density for Cu wires. Figure 8a,b shows the SEM images of 4h-400°C-CuO NWs on Cu mesh, in which there is uniform growth on all surfaces of Cu wires in the Cu mesh, and NWs are approximately vertical to the surface. Like on Cu foil, three different parallel copper oxide layers form on the Cu mesh. SEM images of ZnO/CuO b-NWs on Cu mesh with 4h-400°C-CuO NW cores and for two different ZnO growth times ((c and d)
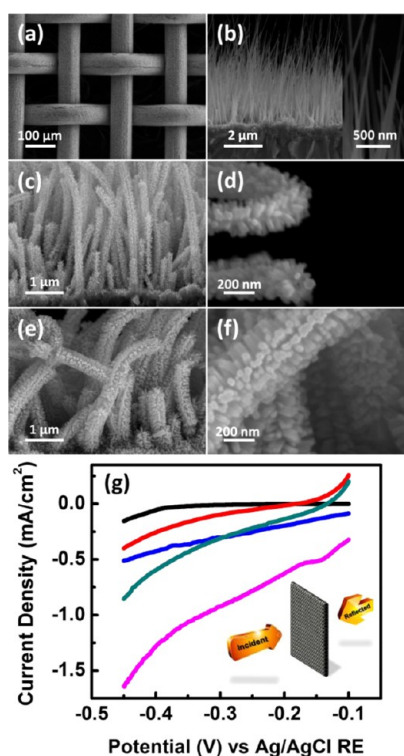
Figure 8. (a and b) SEM images of 4h-400°C-CuO NWs on Cu mesh. The inset in (b) shows high-magnification image illustrating the CuO NWs diameter size. SEM images of ZnO/CuO b-NWs grown on Cu mesh with 4h-400°C-CuO NW cores and different ZnO NW branches ((c and d) 5m-ZnO and (e and f) 10m-ZnO). (g) Current density of b(10m-ZnO/3h-400°C-CuO) NWs on Cu foil (black line, dark current; blue line, light current) and on Cu mesh (red line, dark current; dark cyan line, light current; magenta line, light current with the reflector). Inset shows a schematic of mesh sample with incident and reflected light illuminating both sides of the mesh.

5m and (e and f) 10m) are exhibited in Figure 8c—f, in which ZnO/CuO b-NWs on mesh show the same characteristics as those described earlier for Cu foil (see also Figures S10a—c).

The current densities of b(10m-ZnO/3h-400°C-CuO) NWs grown on different Cu substrates (foil and mesh) are shown in Figure 8g. Due to the increased surface area caused by the mesh substrate, the dark and light currents of b-NWs on Cu mesh are higher than those on Cu foil. To use both sides of mesh, an aluminum reflector (which was angled a little during the $J-V$ measurement) was used to reflect the incident light and illuminate the back of mesh (see Figure 8g inset). As shown, the light current of b-NWs on mesh significantly increases after using the reflector. Photocathode energy

conversion efficiency[31] of b-NWs on mesh with the reflector is much higher than that on foil due to much enhanced photocurrent (light current − dark current). Connecting two mesh samples together and illuminating both sides of the connected sample can further increase the photocathode conversion efficiency.

Although our reported ZnO/Si b-NWs show high hydrogen production efficiency, they require high biasing potential to drive water splitting.[22,31] In this regard, the ZnO/CuO b-NWs can be more promising because they are photoactive at low biasing potentials. The main challenge to use the ZnO/CuO b-NWs for efficient/practical hydrogen production is long-term stability since both CuO and ZnO NWs are not stable over long time resulting in photocurrent degradation for b-NWs over time (Figure 5f,i). To improve the stability of ZnO/CuO b-NW photoelectrodes and obtain long-term stability, a decomposition/dissolution-resistant coating layer such as TiO_2 can be used to protect the b-NWs.[31] Using such a coating strategy, we have shown stability of over one day under constant light illumination for the TiO_2/Pt coated ZnO/Si b-NWs.[32]

CONCLUSIONS

In summary, we showed the facile and large-scale fabrication of 3D ZnO/CuO b-NW photocathodes for solar hydrogen production in a neutral electrolyte. The ZnO/CuO b-NWs were grown on different copper substrates for different ZnO and CuO NWs sizes and densities applying simple, cost-effective thermal oxidation and hydrothermal growth methods. The b-NWs were characterized in detail using high-resolution scanning and transmission electron microscopies showing single-crystalline defect-free b-NWs with smooth and clean surfaces. The b-NWs with longer and denser CuO NW cores exhibited higher photocathodic current due to increased surface area. The ZnO/CuO b-NWs presented higher photocurrent than the CuO/ZnO cs-NWs because of increased surface area and improved gas evolution. The ZnO/CuO b-NWs showed a broadband photoresponse from UV to near IR region. The ZnO/CuO b-NWs grown on the copper mesh exhibited a significantly improved photocathodic current than those grown on the copper film due to improved surface area caused by the mesh substrate. These results provide useful insights in the design and fabrication of unique 3D b-NWs mesh electrodes based on low-cost and earth abundant materials for potential cost-effective and high-efficiency solar fuel production.

METHODS

ZnO/CuO b-NWs Synthesis. The CuO NW arrays were grown on different copper substrates (copper foils and meshes) using thermal oxidation growth method.[40] The number of meshes in the Cu mesh substrates was 200 (TWP, Inc.). First, small pieces (~1 cm²) of Cu foils and meshes were cut and cleaned by

sonication in acetone, isopropyl alcohol (IPA), and deionized (DI) water for 5 min each case, consecutively and finally rinsed with DI water and dried with N_2 flow. Then, they were immediately transferred into an open furnace (without using any gas flow) and annealed under air at different temperatures and for various times. The annealing procedure was performed as follows: the furnace temperature was raised to the desirable

temperature (400, 450, or 500 °C) for 10 min and at each annealing temperature, samples were kept at this temperature for the desirable time (2, 3, 4, or 5 h); finally the furnace was gradually cooled down without opening the furnace, and the samples were removed. Note that for both foil and mesh samples, CuO NWs grew on both sides of the Cu substrates due to exposure to oxygen during annealing. The CuO NW substrates were then transferred into the sputtering machine to deposit a thin ZnO seeding layer for the ZnO NW growth using RF magnetron sputtering using a 99.99% ZnO target and in argon gas. The sputtering pressure was 2.5 mT during the deposition. The measured thickness of sputtered ZnO on a glass slide was ∼69 nm. Note that the actual thickness of sputtered ZnO on CuO NWs is smaller than this thickness (see text). For the mesh samples, both sides of the mesh substrates were coated with the ZnO seeding layer. Finally, the ZnO NW branches were grown on the CuO NW cores using identical hydrothermal growth method as reported previously.[32] Note that for the mesh samples, ZnO NWs uniformly grew on all surfaces of Cu wires in the mesh since ZnO seeding layer covered all surfaces on both sides of the mesh. The synthesized b-NW samples were then stored under vacuum for the next processes such as morphology study and PEC tests.

Structural Characterization. A Philips XL30 field-emission environmental scanning electron microscope (ESEM), working at an accelerating voltage of 10.0 kV, was used to obtain the SEM images to study the samples morphologies. The atomic-scale structural analyses were performed using high resolution transmission electron microscopy (HRTEM, JEOL JEM3100F) operated at 300 kV. For further study, spherical aberration-corrected scanning transmission electron microscopy (Cs-corr. STEM, JEOL JEM2100F) operated at 200 kV was employed to identify the actual atomic configuration of NWs. For the TEM sample preparation, the copper foil containing CuO NWs was held with a tweezer and scraped it onto a holey carbon grid to pull out NWs to be attached onto a grid.

Photoelectrochemical and IPCE Measurements. To perform the PEC tests, first the back side of foil samples were completely scratched to have Cu surface because there was CuO NW growth on both sides of the Cu foil, while for mesh samples, only one edge was cleaned. The foil samples were then bonded to Cu wire at the back using indium, which provides an ohmic contact. The edges and backside of foil samples were sealed using epoxy (see Figure S11). For mesh samples, the cleaned edge was only connected to the Cu wire and sealed by epoxy (see Figure S11). A three-electrode PEC cell using a 400 mL aqueous solution of 0.25 M Na_2SO_4 buffered at pH = 7.25 (neutral solution) with Phosphate Buffered Saline (PBS, Sigma) (DI water; 17.6−17.9 MΩ·cm) was used to carry out the current density measurements. The cs-NW or b-NW substrate as working electrode (WE), Pt coil as counter electrode (CE), and Ag/AgCl (1 M KCl) as reference electrode (RE) were the three electrodes in the PEC cell. Illumination was provided by a solar simulator (Newport 67015) using a 150 W xenon lamp and equipped with 1.5 AM filter. Light power intensity was ∼109 mW/cm^2 at the samples position. A potentiostat (Digi-Ivy, Inc.) was used to collect the current density measurements. A scan rate of 5 mV/s was used for the linear sweep voltammetry (LSV) ($J−V$ measurement). A mild agitation was used during the PEC tests and the electrolyte was purged with N_2 gas for at least 5 min before start of each PEC test. For spectral photoresponse and IPCE measurements, a monochromator (iHR 550) with the solar simulator (equipped with 1.5 AM filter) as the light source was used. A silicon photodiode (Newport 818-UV) was used to calibrate the monochromatic light spectrum. Spectral photoresponse and IPCE measurements were performed in the same setup and electrolyte as used for the current density measurements. All the external biasing potentials here are *versus* Ag/AgCl RE, unless otherwise stated.

Conflict of Interest: The authors declare no competing financial interest.

Supporting Information Available: Field-effect mobility measurement and additional supporting images/figures. This material is available free of charge *via* the Internet at http://pubs.acs.org.

REFERENCES AND NOTES

1. Paracchino, A.; Laporte, V.; Sivula, K.; Grätzel, M.; Thimsen, E. Highly Active Oxide Photocathode for Photoelectrochemical Water Reduction. *Nat. Mater.* **2011**, *10*, 456–461.
2. Kay, A.; Cesar, I.; Grätzel, M. New Benchmark for Water Photooxidation by Nanostructured α-Fe₂O₃ Films. *J. Am. Chem. Soc.* **2006**, *128*, 15714–15721.
3. Chen, X.; Liu, L.; Yu, P. Y.; Mao, S. S. Increasing Solar Absorption for Photocatalysis with Black Hydrogenated Titanium Dioxide Nanocrystals. *Science* **2011**, *331*, 746–750.
4. Su, J.; Feng, X.; Sloppy, J. D.; Guo, L.; Grimes, C. A. Vertically Aligned WO₃ Nanowire Arrays Grown Directly on Transparent Conducting Oxide Coated Glass: Synthesis and Photoelectrochemical Properties. *Nano Lett.* **2010**, *11*, 203–208.
5. Wang, G.; Ling, Y.; Wang, H.; Yang, X.; Wang, C.; Zhang, J. Z.; Li, Y. Hydrogen-Treated WO₃ Nanoflakes Show Enhanced Photostability. *Energy Environ. Sci.* **2012**, *5*, 6180–6187.
6. Qiu, Y.; Yan, K.; Deng, H.; Yang, S. Secondary Branching and Nitrogen Doping of ZnO Nanotetrapods: Building a Highly Active Network for Photoelectrochemical Water Splitting. *Nano Lett.* **2011**, *12*, 407–413.
7. Paracchino, A.; Mathews, N.; Hisatomi, T.; Stefik, M.; Tilley, S. D.; Gratzel, M. Ultrathin Films on Copper(i) Oxide Water Splitting Photocathodes: A Study on Performance and Stability. *Energy Environ. Sci.* **2012**, *5*, 8673–8681.
8. Warren, S. C.; Thimsen, E. Plasmonic Solar Water Splitting. *Energy Environ. Sci.* **2012**, *5*, 5133–5146.
9. Ling, Y.; Wang, G.; Reddy, J.; Wang, C.; Zhang, J. Z.; Li, Y. The Influence of Oxygen Content on the Thermal Activation of Hematite Nanowires. *Angew. Chem., Int. Ed.* **2012**, *51*, 4074–4079.
10. Wang, G.; Wang, H.; Ling, Y.; Tang, Y.; Yang, X.; Fitzmorris, R. C.; Wang, C.; Zhang, J. Z.; Li, Y. Hydrogen-Treated TiO₂ Nanowire Arrays for Photoelectrochemical Water Splitting. *Nano Lett.* **2011**, *11*, 3026–3033.
11. Zhao, X.; Wang, P.; Li, B. CuO/ZnO Core/Shell Heterostructure Nanowire Arrays: Synthesis, Optical Property, and Energy Application. *Chem. Commun.* **2010**, *46*, 6768–6770.
12. Jin, W.-M.; Kang, J.-H.; Moon, J. H. Fabrication of 3D Copper Oxide Structure by Holographic Lithography for Photoelectrochemical Electrodes. *ACS Appl. Mater. Interfaces* **2010**, *2*, 2982–2986.
13. Chiang, C.-Y.; Epstein, J.; Brown, A.; Munday, J. N.; Culver, J. N.; Ehrman, S. Biological Templates for Antireflective Current Collectors for Photoelectrochemical Cell Applications. *Nano Lett.* **2012**, *12*, 6005–6011.
14. Tilley, S. D.; Cornuz, M.; Sivula, K.; Grätzel, M. Light-Induced Water Splitting with Hematite: Improved Nanostructure and Iridium Oxide Catalysis. *Angew. Chem., Int. Ed.* **2010**, *49*, 6405–6408.
15. Salvador, P. Hole Diffusion Length in n-TiO₂ Single Crystals and Sintered Electrodes: Photoelectrochemical Determination and Comparative Analysis. *J. Appl. Phys.* **1984**, *55*, 2977–2985.
16. Sivula, K.; Zboril, R.; Le Formal, F.; Robert, R.; Weidenkaff, A.; Tucek, J.; Frydrych, J.; Grätzel, M. Photoelectrochemical Water Splitting with Mesoporous Hematite Prepared by a Solution-Based Colloidal Approach. *J. Am. Chem. Soc.* **2010**, *132*, 7436–7444.
17. de Jongh, P. E.; Vanmaekelbergh, D.; Kelly, J. J. Cu₂O: Electrodeposition and Characterization. *Chem. Mater.* **1999**, *11*, 3512–3517.

18. Hendry, E.; Koeberg, M.; O'Regan, B.; Bonn, M. Local Field Effects on Electron Transport in Nanostructured TiO_2 Revealed by Terahertz Spectroscopy. *Nano Lett.* **2006**, *6*, 755–759.

19. Ling, Y.; Wang, G.; Wheeler, D. A.; Zhang, J. Z.; Li, Y. Sn-Doped Hematite Nanostructures for Photoelectrochemical Water Splitting. *Nano Lett.* **2011**, *11*, 2119–2125.

20. Seabold, J. A.; Choi, K.-S. Effect of a Cobalt-Based Oxygen Evolution Catalyst on the Stability and the Selectivity of Photo-Oxidation Reactions of a WO_3 Photoanode. *Chem. Mater.* **2011**, *23*, 1105–1112.

21. Dare-Edwards, M. P.; Goodenough, J. B.; Hamnett, A.; Trevellick, P. R. Electrochemistry and Photoelectrochemistry of Iron(III) Oxide. *J. Chem. Soc., Faraday Trans. 1* **1983**, *79*, 2027–2041.

22. Sun, K.; Jing, Y.; Li, C.; Zhang, X.; Aguinaldo, R.; Kargar, A.; Madsen, K.; Banu, K.; Zhou, Y.; Bando, Y.; *et al.* 3D Branched Nanowire Heterojunction Photoelectrodes for High-Efficiency Solar Water Splitting and H_2 Generation. *Nanoscale* **2012**, *4*, 1515–1521.

23. Yang, X.; Wolcott, A.; Wang, G.; Sobo, A.; Fitzmorris, R. C.; Qian, F.; Zhang, J. Z.; Li, Y. Nitrogen-Doped ZnO Nanowire Arrays for Photoelectrochemical Water Splitting. *Nano Lett.* **2009**, *9*, 2331–2336.

24. Cho, I. S.; Chen, Z.; Forman, A. J.; Kim, D. R.; Rao, P. M.; Jaramillo, T. F.; Zheng, X. Branched TiO_2 Nanorods for Photoelectrochemical Hydrogen Production. *Nano Lett.* **2011**, *11*, 4978–4984.

25. Su, J.; Guo, L.; Bao, N.; Grimes, C. A. Nanostructured WO_3/$BiVO_4$ Heterojunction Films for Efficient Photoelectrochemical Water Splitting. *Nano Lett.* **2011**, *11*, 1928–1933.

26. Hansen, B. J.; Kouklin, N.; Lu, G.; Lin, I. K.; Chen, J.; Zhang, X. Transport, Analyte Detection, and Opto-Electronic Response of p-Type CuO Nanowires. *J. Phys. Chem. C* **2010**, *114*, 2440–2447.

27. Zhang, Z.; Wang, P. Highly Stable Copper Oxide Composite as an Effective Photocathode for Water Splitting *via* a Facile Electrochemical Synthesis Strategy. *J. Mater. Chem.* **2012**, *22*, 2456–2464.

28. Kargar, A.; Partokia, S. S.; Allameh, P.; May, S.; Niu, M.; Sun, K.; Yang, M.; Wang, D. Solution-Grown 3D Cu_2O Networks for Efficient Solar Water Splitting. Submitted to *Nanotechnol.*, **2013**.

29. Siripala, W.; Ivanovskaya, A.; Jaramillo, T. F.; Baeck, S.-H.; McFarland, E. W. A Cu_2O/TiO_2 Heterojunction Thin Film Cathode for Photoelectrocatalysis. *Sol. Energy Mater. Sol. Cells* **2003**, *77*, 229–237.

30. Cheng, C.; Fan, H. J. Branched Nanowires: Synthesis and Energy Applications. *Nano Today* **2012**, *7*, 327–343.

31. Kargar, A.; Sun, K.; Jing, Y.; Choi, C.; Jeong, H.; Jung, G. Y.; Jin, S.; Wang, D. 3D Branched Nanowire Photoelectrochemical Electrodes for Efficient Solar Water Splitting. *ACS Nano* **2013**, *7*, 9407–9415.

32. Kargar, A.; Sun, K.; Jing, Y.; Choi, C.; Jeong, H.; Zhou, Y.; Madsen, K.; Naughton, P.; Jin, S.; Jung, G. Y.; *et al.* Tailoring n-ZnO/p-Si Branched Nanowire Heterostructures for Selective Photoelectrochemical Water Oxidation or Reduction. *Nano Lett.* **2013**, *13*, 3017–3022.

33. Song, H. S.; Zhang, W. J.; Cheng, C.; Tang, Y. B.; Luo, L. B.; Chen, X.; Luan, C. Y.; Meng, X. M.; Zapien, J. A.; Wang, N.; *et al.* Controllable Fabrication of Three-Dimensional Radial ZnO Nanowire/Silicon Microrod Hybrid Architectures. *Cryst. Growth Des.* **2010**, *11*, 147–153.

34. Kronawitter, C. X.; Vayssieres, L.; Shen, S.; Guo, L.; Wheeler, D. A.; Zhang, J. Z.; Antoun, B. R.; Mao, S. S. A Perspective on Solar-Driven Water Splitting with All-Oxide Hetero-Nanostructures. *Energy Environ. Sci.* **2011**, *4*, 3889–3899.

35. Yin, Z.; Wang, Z.; Du, Y.; Qi, X.; Huang, Y.; Xue, C.; Zhang, H. Full Solution-Processed Synthesis of All Metal Oxide-Based Tree-like Heterostructures on Fluorine-Doped Tin Oxide for Water Splitting. *Adv. Mater.* **2012**, *24*, 5374–5378.

36. Lu, X.; Wang, G.; Xie, S.; Shi, J.; Li, W.; Tong, Y.; Li, Y. Efficient Photocatalytic Hydrogen Evolution over Hydrogenated ZnO Nanorod Arrays. *Chem. Commun.* **2012**, *48*, 7717–7719.

37. Guo, Z.; Chen, X.; Li, J.; Liu, J.-H.; Huang, X.-J. ZnO/CuO Hetero-Hierarchical Nanotrees Array: Hydrothermal Preparation and Self-Cleaning Properties. *Langmuir* **2011**, *27*, 6193–6200.

38. Zhou, W.; Cheng, C.; Liu, J.; Tay, Y. Y.; Jiang, J.; Jia, X.; Zhang, J.; Gong, H.; Hng, H. H.; Yu, T.; *et al.* Epitaxial Growth of Branched α-Fe_2O_3/SnO_2 Nano-Heterostructures with Improved Lithium-Ion Battery Performance. *Adv. Funct. Mater.* **2011**, *21*, 2439–2445.

39. Cheng, C.; Liu, B.; Yang, H.; Zhou, W.; Sun, L.; Chen, R.; Yu, S. F.; Zhang, J.; Gong, H.; Sun, H.; *et al.* Hierarchical Assembly of ZnO Nanostructures on SnO_2 Backbone Nanowires: Low-Temperature Hydrothermal Preparation and Optical Properties. *ACS Nano* **2009**, *3*, 3069–3076.

40. Jiang, X.; Herricks, T.; Xia, Y. CuO Nanowires Can Be Synthesized by Heating Copper Substrates in Air. *Nano Lett.* **2002**, *2*, 1333–1338.

41. Goncalves, A. M. B.; Campos, L. C.; Ferlauto, A. S.; Lacerda, R. G. On the Growth and Electrical Characterization of CuO Nanowires by Thermal Oxidation. *J. Appl. Phys.* **2009**, *106*, 034303.

42. Sun, K.; Jing, Y.; Park, N.; Li, C.; Bando, Y.; Wang, D. Solution Synthesis of Large-Scale, High-Sensitivity ZnO/Si Hierarchical Nanoheterostructure Photodetectors. *J. Am. Chem. Soc.* **2010**, *132*, 15465–15467.

43. Garnett, E.; Yang, P. Light Trapping in Silicon Nanowire Solar Cells. *Nano Lett.* **2010**, *10*, 1082–1087.

44. Law, M.; Greene, L. E.; Johnson, J. C.; Saykally, R.; Yang, P. Nanowire Dye-Sensitized Solar Cells. *Nat. Mater.* **2005**, *4*, 455–459.

45. Zainelabdin, A.; Zaman, S.; Amin, G.; Nur, O.; Willander, M. Optical and Current Transport Properties of CuO/ZnO Nanocoral p−n Heterostructure Hydrothermally Synthesized at Low Temperature. *Appl. Phys. A: Mater. Sci. Process.* **2012**, *108*, 921–928.

46. Wang, P.; Zhao, X.; Li, B. ZnO-coated CuO Nanowire Arrays: Fabrications, Optoelectronic Properties, and Photovoltaic Applications. *Opt. Express* **2011**, *19*, 11271–11279.

47. Jung, S.; Yong, K. Fabrication of CuO-ZnO Nanowires on a Stainless Steel Mesh for Highly Efficient Photocatalytic Applications. *Chem. Commun.* **2011**, *47*, 2643–2645.